

CHAPTER 11

EMD AND INSTANTANEOUS PHASE DETECTION OF STRUCTURAL DAMAGE

Liming W. Salvino, Darryll J. Pines, Michael Todd and Jonathan M. Nichols

In this chapter, a new structural health-monitoring and damage-detection method is presented. A general time-frequency data analysis technique (empirical mode decomposition and the Hilbert–Huang spectrum) in conjunction with a wave-mechanics-based concept is developed to provide a diagnostic tool for detecting and interpreting adverse changes in a structure. Sets of simple basis function components, known as intrinsic mode functions (IMF), are extracted adaptively from the measured structural response time series data. These IMFs are amplitude- and phase-modulated signals and are used to define the instantaneous phases of structural waves. The state of a structure is evaluated, and damage is identified based on these instantaneous phase features. Furthermore, fundamental relationships are developed connecting the instantaneous phases to a local physics-based structural representation in order to infer damage in terms of physical parameters, such as structural mass, stiffness, and damping. Damage-detection applications are investigated by using numerical simulations and a variety of laboratory experiments with simple structures. Several different types of excitation mechanisms are used for dynamic input to the structures. The time series output of the structural response is then analyzed by using the new method. The instantaneous phase relationships are extracted and examined for changes which may have occurred due to damage. These results are compared to those from other newly developed detection methods, such as an algorithm based on the geometric properties of a chaotic attractor. The studies presented here show that our method, without linear-system or stationary-process assumptions, can identify and locate structural damage and permit the further development of a reliable real-time structural health-monitoring and damage-detection system.

11.1. Introduction to structural health monitoring

The nondestructive evaluation and monitoring of the health of a large and complex structure and its components are of great interest to the aerospace, defense, civil, mechanical, and marine engineering communities. One of the key goals of a comprehensive structural health monitoring (SHM) system is the ability to identify a structural anomaly at the earliest possible stage and to evaluate the behavior of the structure as damage accumulates. Almost all damage-detection methods currently in use are either visual or localized experimental methods, such as acoustic or ultrasonic techniques. These local detection methods are not only time-consuming to

perform, but also require the general location of the damage to be known in advance and the structure to be taken out of service for inspection. The need for an effective and robust diagnostic method that can be applied to complex structures has led to the development of global detection methods which examine changes in the measured vibration characteristics of the structure. The basic premise of global damage-identification methods is that damage will alter the stiffness, mass, or damping properties of a system, and that this change, in turn, will alter the measured dynamic response of the structure.

The traditional approach of a global method is to examine changes in modal properties or changes in quantities derived from modal properties. The central idea of modal methods is that a change in a structure, such as damage, should imply a change in the modal parameters of the structure, such as frequencies, damping, mode shapes, and mode shape curvatures. These techniques are usually based on classical linear theory, and most studies assume that the structure can be modeled as a linear system before and after damage. In general, these modal techniques have not been widely accepted for practical monitoring applications due to their insensitivity to localized damage, linearity assumptions, boundary conditions, sensitivity to sensor locations, and other environmental effects. To overcome these fundamental limitations of the modal method, an extensive amount of research in recent years has been associated with the development of other diagnostic and prognostic methods and algorithms. A review of these many techniques and their applications can be found in Doebling et al. (1996, 1998) and Chang (2001, 2003).

The use of an empirical or data-driven approach, intended to assess the state of a structure from measured structural responses, is rapidly developing and increasing in popularity. Rather than fitting the data to a specific analytical model of a structure whose true complexity is extremely difficult to capture mathematically, one uses measured data, collected from a structural response at some reference state, as an undamaged baseline or empirical model of the structure. When damage occurs and progresses, the dynamic behavior of the structure will differ from that of the baseline empirical model. Certain features can then be chosen to measure this discrepancy, detect damage, and evaluate the structural state. For example, the damage-detection method introduced here uses the instantaneous phase of measured structural waveforms as indicators of damage. Another example of a recently developed method uses a prediction error, a concept taken from the nonlinear dynamics community, as the damage indicator (see subsection 11.4.5). Direct comparisons between some of these methods will be given and further discussed in section 11.4.

Another popular approach is a wavelet-based damage-detection method. Wavelet analysis permits vibration signals from structures to be decomposed into fundamental basis functions that are used to characterize the vibration response. By tracking changes in these fundamental basis functions, structural defects can be detected by inspecting the time-frequency properties of the vibration signal. However, a disadvantage of current wavelet-based diagnostic algorithms is the use of currently

available wavelet dictionaries, which are not necessarily appropriate for analyzing the behavior of a particular structural system. In addition, wavelet methods, designed to accommodate the transient nature of the data, may not work well if the underlying physical process cannot be approximated by linear processes. Finally, another time domain method is auto-regressive (AR) modeling, which also assumes that a measured response coming from a structure can be accurately represented by a linear model. The AR model and an example of damage detection using the AR model are presented in subsection 11.4.4.

The effects of damage on a structure can be classified as linear or nonlinear. Nonlinear damage, defined as the case when the initially linear-elastic structure behaves in a nonlinear manner after the damage has been introduced, is ubiquitous in nature. A robust damage-detection method must be applicable to, or at least sensitive to, both these general types of damage. Because of the inherent difficulty of analyzing nonlinear processes, the vast majority of past and even most present works address only the problem of linear damage detection.

In this chapter, we discuss a fundamentally new data-driven approach where damage features are identified and evaluated based on the instantaneous phases of structural waves. This approach is implemented by means of the empirical mode decomposition (EMD) and Hilbert–Huang spectrum technique (Huang et al. 1998). Instantaneous phases are defined by utilizing the unique characteristics of intrinsic mode functions (IMFs), which are amplitude- and phase-modulated basis functions extracted directly from the measured signal. In addition, this IMF function representation is coupled with a local physics-based model of structures in order to infer damage in terms of physical parameters, such as structural mass, stiffness, and damping. Based on the intrinsic nature of the EMD method, this approach does not assume a linear system or a stationary process for the measured data.

The success of SHM and damage-detection methodologies involves many important issues such as excitation and measurement considerations, including the selection of types and locations of sensors and excitations. The examples used in this chapter to demonstrate EMD and instantaneous phase damage detection include several different types of excitation mechanisms such as a broadband noise or random excitations, deterministic chaos signals, as well as realistic signals recorded during an earthquake event. The results of these studies show that our method and algorithm perform well without any knowledge of excitation sources. The detailed description of the phase detection method and the results for several examples will be given in sections 11.3 and 11.4. We begin the discussion in the next section by introducing the concept of “instantaneous phase” and the method used to extract it from a measured time series in order to describe the dynamics of a structural system.

11.2. Instantaneous phase and EMD

The fundamental physical quantities of a structural system, such as acceleration, strain, and pressure, can be obtained through measurements of the time waveforms, which are denoted by time series data or the signal of $x(t)$. In principle, such signals can have any functional form and most likely will have extraordinary richness and complexity. One of the logical attempts to express such signals is to generalize the simplicity of the sinusoid functions with the time-dependent variables

$$x(t) = a(t) \cos[\theta(t)], \quad (11.1)$$

where the amplitude $a(t)$ and phase $\theta(t)$ are arbitrary functions of time. To emphasize that they generally change in time, the terms “amplitude modulation” and “phase modulation” are often used. Difficulties arise immediately. Nature gives us only the left side of (11.1). How do we break up a signal in terms of time-dependent amplitude and phase? Moreover, even if the data were generated numerically by way of (11.1) with chosen $a(t)$ and $\theta(t)$, the choices are somewhat arbitrary because there are an infinite number of ways of choosing different pairs of amplitudes and phases that generate the same data $x(t)$. How do we unambiguously define an amplitude and phase? Why is a complex signal used, and how do we define a complex signal corresponding to a real signal? The general mathematical background needed to address these questions as well as the development of an analytic signal and its equations can be found in Cohen (1995).

The focus in this section is to utilize the mathematical groundwork given in Cohen (1995) and further impose constraints such that the phase function $\theta(t)$ can be used as a generalized angle associated with the time evolution of the dynamic system in space to describe structural waves. In the context of wave propagation, the time-dependent phase angle should be one of the important quantities for a variety of engineering applications. Unfortunately, the phase information is often ignored mainly because of a fundamental problem associated with extracting phases from measured data by way of the analytic signal without the important constraint. This topic will be the subject of discussion in the next few subsections.

11.2.1. Instantaneous phase

An instantaneous phase $\theta(t)$ can be defined by the analytic signal $z(t)$,

$$z(t) = x(t) + i \mathcal{H}[x(t)] = a(t)e^{i\theta(t)}, \quad (11.2)$$

where the given time series $x(t)$ is the real part of (11.2), and the imaginary part is the Hilbert transform of $x(t)$,

$$\mathcal{H}[x(t)] = \frac{1}{\pi} \text{PV} \int_{-\infty}^{\infty} \frac{x(\tau)}{t - \tau} d\tau. \quad (11.3)$$

In (11.3), PV denotes the Cauchy principal value of the integral. An analytic signal represents a rotation in the complex plane with the radius of rotation $a(t)$ and the instantaneous phase angle $\theta(t)$, where

$$a(t) = \sqrt{[x(t)]^2 + \{\mathcal{H}[x(t)]\}^2} \quad \text{and} \quad \theta(t) = \arctan\left\{\frac{\mathcal{H}[x(t)]}{x(t)}\right\}. \quad (11.4)$$

To uniquely describe the time evolution of a dynamic system flow such as a measured structural response, the phase functions need to be restricted to a definite evolving direction (e.g., either clockwise or counterclockwise) and a unique center of rotation at any time t . This requirement guarantees that the instantaneous angular velocity $\omega(t)$ of the rotation

$$\omega(t) = \frac{d\theta(t)}{dt} = 2\pi f(t), \quad (11.5)$$

or instantaneous frequency $f(t)$ remains positive for all time t . Obviously, only a positive $f(t)$ can be physically meaningful and can be used to construct the time-frequency spectrum.

A fundamental difficulty in defining an instantaneous phase $\theta(t)$ by using (11.2) and (11.3) based on a measured time series data $x(t)$ is that $\theta(t)$ may exhibit different evolving directions in the complex plane and/or multiple centers of rotations, even for simple continuous dynamic system flows. For example, the numerical solutions of the Lorenz system of equations,

$$\begin{aligned} \dot{y}_1 &= 16(y_2 - y_1) \\ \dot{y}_2 &= 40y_1 - y_2 + y_1y_3 \\ \dot{y}_3 &= -4y_3 + y_1y_2, \end{aligned} \quad (11.6)$$

given in Fig. 11.1 illustrate this difficulty. Figure 11.1a is the output time series $x(t) \equiv y_1(t)$, and Fig. 11.1 shows its trajectory in the complex plane of $z(t)$, which is the analytic signal constructed by using $x(t)$.

No phase function can be properly defined for the rotation characteristics displayed in Fig. 11.1b. A phase function obtained directly from the analytic signal does not uniquely represent the time evolution of the dynamics. Further explanations and examples of such phase characteristics will be given in subsection 11.2.3. This problem remains unsolved without the introduction of a special type of function, the intrinsic mode function (IMF). An IMF is a key concept associated with the method of EMD and Hilbert–Huang transform (HHT).

11.2.2. EMD and HHT

The empirical mode decomposition and Hilbert–Huang transform is a general time-frequency method, which consists of two stages in analyzing time series data. The first stage involves the use of EMD, which decomposes any given time series data into a set of simple oscillatory functions, defined as intrinsic mode functions (IMFs).

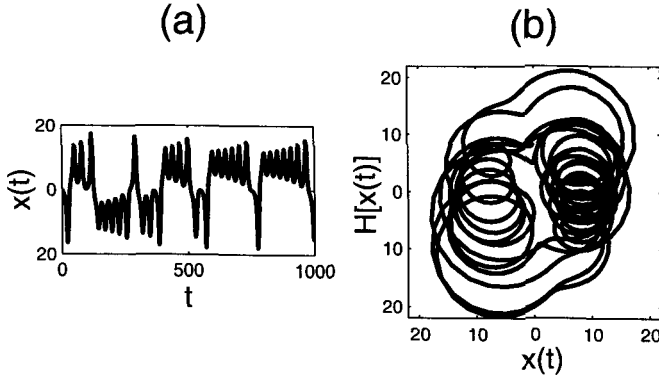


Figure 11.1: (a) Lorenz chaotic time series and (b) Lorenz trajectory in the complex plane.

An IMF must satisfy the conditions that a number of extrema must be equal to the number of zero crossings (or differ by one at most), and the mean value of the envelope functions, defined by local extrema, must be zero. The IMF components can be obtained by a repeated application of an iterative procedure called “sifting.” For example, the first IMF $c_1(t) = \text{sifting}[x(t)]$ can be obtained by sifting the $x(t)$, where $x(t)$ is the measured time series data. The second IMF is then equal to $c_2(t) = \text{sifting}[x(t) - c_1(t)]$, and so on. As a result,

$$x(t) = \sum_{k=0}^n c_k(t); \quad (11.7)$$

that is, the measured time series data can be decomposed into n empirical modes, each satisfying the conditions of an IMF, plus a residual term $c_0(t)$. In general, n is a small number (often less than 10). This method of decomposition is very efficient. The decomposition base is directly derived from the data and is established from a simple assumption that any data consist of different intrinsic modes of oscillation. As a result, each IMF is an amplitude- and frequency-modulated signal; i.e.,

$$c_k(t) = a_k(t) \cos[\theta_k(t)]. \quad (11.8)$$

By these criteria, $c_k(t)$ is a mono-component signal (Cohen 1995), which has a monotonically increasing phase and a positive instantaneous frequency. A complete description of the sifting procedure can be found in Huang et al. (1998), and examples of $c_k(t)$ obtained from the structural response of an undamaged structure in comparison with that of a damaged structure are given in later subsections.

The second stage of the method defines the time-dependent amplitudes (or energies) and frequencies of the empirical modes by using a Hilbert transform. For a given $c_k(t)$, an analytic signal $z_k(t)$ can then be defined by using the k th IMF component $c_k(t)$ and its Hilbert transform $d_k(t) = \mathcal{H}[c_k(t)]$. An instantaneous amplitude and frequency can then be defined accordingly by using (11.4) and (11.5).

For simplicity, the mode index k is omitted in all equations and text below.

The instantaneous (time-dependent) frequency defined by this approach is based on the local oscillation over a characteristic time scale of the measured data, which is represented by n empirical modes, and the time derivative of its phase relationship is obtained from the Hilbert transform. This approach is fundamentally different compared to the conventional Fourier transform and Fourier representation of the frequency domain information.

Because both the amplitude and frequency of each IMF are a function of time, a three-dimensional space or ordered triplet $[t, \omega(t), a(t)]$ can be defined. This space is generalized by means of a function of two variables $H(\omega, t)$ to $[t, \omega, H(\omega, t)]$, where $a(t) = H[\omega(t), t]$. This final representation is referred to as the “Hilbert (amplitude) spectrum” $H(\omega, t)$ in Huang et al. (1998). $H(\omega, t)$ or $H(f, t)$ is also known as the “Hilbert–Huang transformation” or “HHT”. Similarly, the Hilbert energy spectrum can be defined by computing the amplitude squared to represent the energy density if desired. In addition, a Hilbert marginal spectrum $H(\omega)$ can be defined by the integration of $H(\omega, t)$ over the entire data length T . The marginal spectrum $H(\omega)$ or $H(f)$ is a frequency spectrum and measures the total amplitude contribution from each frequency value of the data.

11.2.3. Extracting an instantaneous phase from measured data

As stated in previous subsections, each $\theta(t)$ computed by $c(t)$ exhibits a definite evolving direction, either clockwise or counterclockwise, and a unique center of rotation at any time t . The left column of Fig. 11.2 shows the first four IMFs plotted as a function of time t , computed from the Lorenz output data given in Fig. 11.1a. The right column of Fig. 11.2 shows their corresponding trajectory in the complex plane of $z(t)$, or equivalently, in the polar coordinate $[a(t), \theta(t)]$. Collectively, a total phase function $\theta(t)$ can be defined as

$$\theta(t) = \sum_{k=0}^n \arctan \left\{ \frac{\mathcal{H}[c_k(t)]}{c_k(t)} \right\}. \quad (11.9)$$

While $\theta_k(t)$ [see (11.8)] represents the number of rotations for the k th IMF function, (11.9) gives the total number of rotations of the measured signal $x(t)$ in the complex plane. When $\theta(t)$ is unwrapped with radian phases in time, it assigns the total number of rotations in the complex plane for a unique time value t (multiplied by 2π). To further illustrate the properties of instantaneous phase functions, Fig. 11.3 is used to display $\theta(t)$ by using unwrapped radian phases with changing absolute jumps greater than π to their 2π complements. In Fig. 11.3a, $\theta(t)$, defined directly by the Lorenz output data, is compared with Fig. 11.3b, where $\theta(t)$ is defined by IMF and (11.9). Note the significant difference in vertical axes. In Fig. 11.3a, $\theta(t)$ misrepresents many important local oscillatory modes; i.e., it associates many different intrinsic modes of oscillation with the same time variable. Only in Fig. 11.3b, does

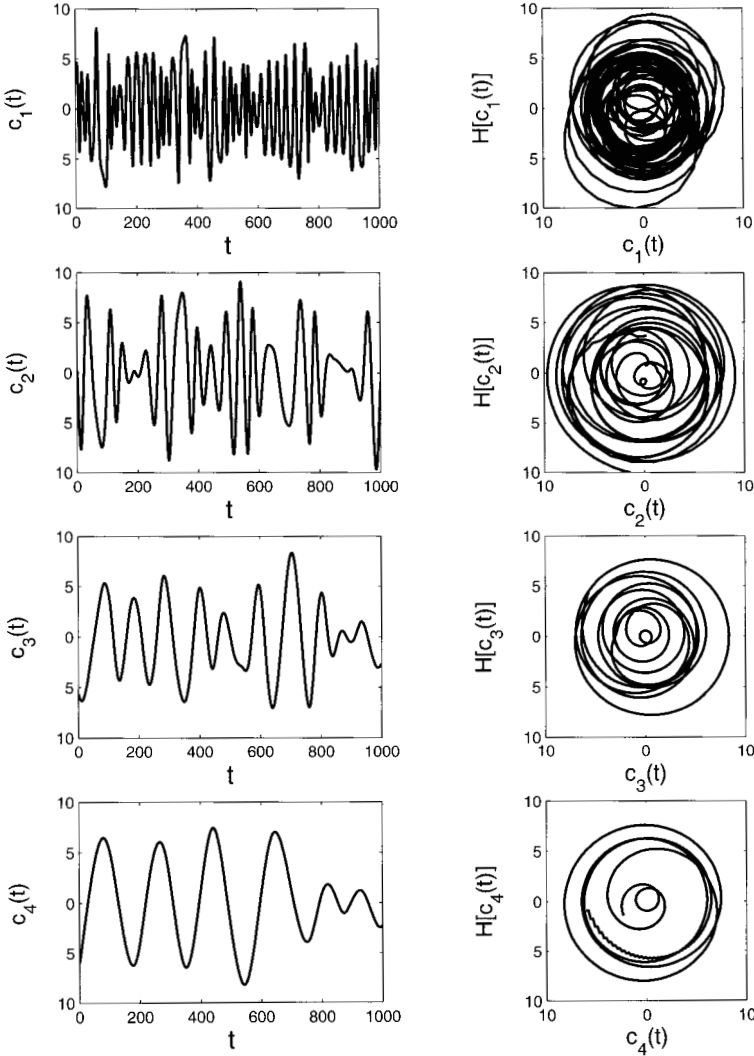


Figure 11.2: The first four IMFs (left column) and their corresponding trajectory in the complex plane (right column).

$\theta(t)$ represent a well-defined phase function with monotonically increasing values for all time t . As a result, this phase function properly represents all local oscillations in the data.

11.3. Damage detection application

An instantaneous phase, defined in (11.9), can be a natural physical variable to describe the dynamics of a system. When this description is applied to a structural system, the phase is interpreted as a generalized angle associated with the time

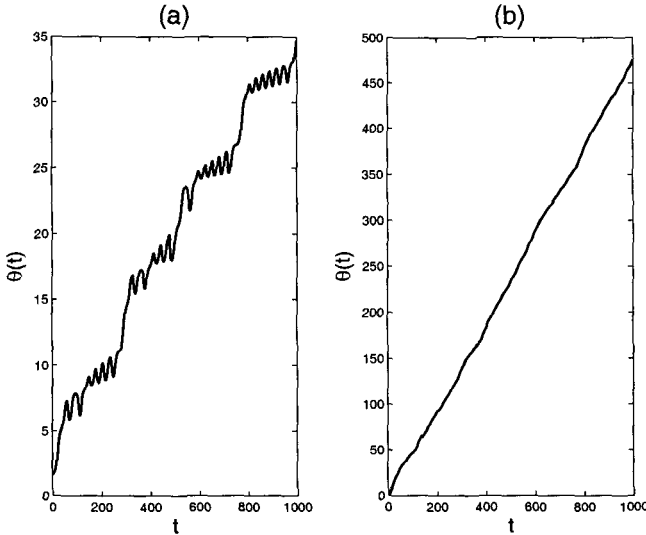


Figure 11.3: (a) $\theta(t)$ computed by the Lorenz data directly (b) $\theta(t)$ obtained by IMF and (11.9).

evolution of a measured structural response. In particular, $\theta(t)$ is used to represent the phase of traveling structural waves of any dynamically measurable quantity, such as the acceleration, strain, or displacement. The value of this phase function at a location p on a structure can be written as $\theta_p(t)$. If point zero on a structure is chosen as a reference point, the phase function relative to the reference point can be defined by

$$\varphi_s(t) = |\theta_p(t) - \theta_0(t)| . \quad (11.10)$$

The variable $\varphi_s(t)$ describes the relative phase relationship of a traveling structural wave for a given state of a structure s . The basic idea of detecting damage by using $\varphi_s(t)$ is that damage in a structure will alter the speed at which energy traverses through the structure. As a result, the $\varphi_s(t)$ values will be altered compared to those of an undamaged state $\varphi_u(t)$, with the damaged state $\varphi_d(t)$ between the same locations p and 0 on the structure. The characteristics of the damage features identified through $\varphi_s(t)$ can then be combined with the concept of phase dereverberation in order to infer damage in terms of physical parameters such as structural stiffness, mass and damping (Purekar and Pines 2000; Ma and Pines 2003). Our previous work has suggested that tracking the changes in the wave speed of response measurements by using (11.10) through each individual structural element between successive degrees of freedom for an impulse excited one-dimensional structure is an effective method for identifying as well as locating damage (Pines and Salvino 2002; Salvino and Pines 2002). A brief description of this approach is given in the next few subsections.

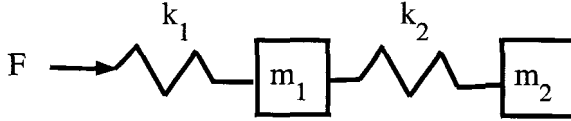


Figure 11.4: Three-degrees of freedom (DOF), one-dimensional spring-mass system.

11.3.1. One-dimensional structures

The concept of phase dereverberation can be interpreted as obtaining the response of a structure to the incident energy imparted to the system. Consider the three-degrees of freedom (DOF) spring-mass system shown in Fig. 11.4.

The equation of motion for this system is given generically by

$$M\ddot{x} + Kx = F, \quad (11.11)$$

where

$$M = \begin{bmatrix} 0 & 0 & 0 \\ 0 & m_1 & 0 \\ 0 & 0 & m_2 \end{bmatrix}, \quad K = \begin{bmatrix} k_1 & -k_1 & 0 \\ -k_1 & k_1 + k_2 & -k_2 \\ 0 & -k_2 & k_2 \end{bmatrix}, \quad \text{and} \quad F = \begin{bmatrix} 1 \\ 0 \\ 0 \end{bmatrix}. \quad (11.12)$$

By using the concept of virtual control, the dereverberated transfer functions can be represented by

$$\begin{bmatrix} u_1/F_1 \\ u_2/F_1 \\ u_3/F_1 \end{bmatrix} = \begin{bmatrix} k_1 & -k_1 & 0 \\ -k_1 & k_1 + k_2 - m_1\omega^2 + G_1 & -k_2 \\ 0 & -k_2 & k_2 - m_2\omega^2 + G_2 \end{bmatrix}^{-1} \begin{bmatrix} 1 \\ 0 \\ 0 \end{bmatrix}. \quad (11.13)$$

The virtual controllers G_1 and G_2 are given by

$$G_1 = k_1(1 - e^{-\mu_1}) - k_2(1 - e^{-\mu_2}), \quad (11.14)$$

and

$$G_2 = k_2(1 - e^{-\mu_2}), \quad (11.15)$$

where μ_1 and μ_2 are the propagation coefficients. An impulse F is applied from the left side, and the baseline system response is simulated by considering parameters $m_1 = m_2 = 1$, $k_1 = 1$, and $k_2 = 2.5$. The damaged cases are generated by reducing the spring constants by 25%, 50% and 75% for each k_1 and k_2 separately. The displacement response of the dereverberated time series at DOF 2 is displayed in Fig. 11.5 comparing baseline and three simulated damage cases in the first structural element with varying spring stiffness k_1 .

For the example given in Fig. 11.5, the time series of the DOF 2 reveals a phase lag associated with the incident impulse as it traverses the structure from left to right. As the stiffness of element 1 decreases, the speed at which energy traverses

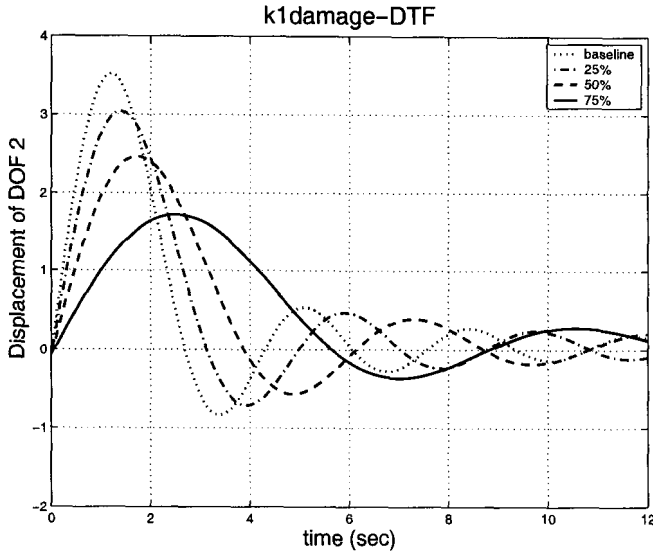


Figure 11.5: Displacement responses for the three DOF system of undamaged and three k_1 -damage cases.

this element decreases. This finding suggests that one approach for determining the presence of damage in a structure is to track the changes in wave speed through each individual structural element between successive degrees of freedom. Thus, one physical approach to damage identification in a system is to use the phase relationship of successive degrees of freedom to track the variation in structural properties.

The simulated time series for the displacement response, as shown in Fig. 11.5, are first decomposed into a set of IMFs. These IMFs are then used in (11.9) to calculate the time-dependent phases of the three DOF spring-mass system. The value of this phase function at DOF 2 is written as $\theta_2(t)$. If DOF 1 is chosen as a reference point, the phase function relative to the reference point can be defined by

$$\varphi_s(t) = |\theta_2(t) - \theta_1(t)|. \quad (11.16)$$

Figure 11.6 illustrates the changes of phase relationship due to the presence of damage in the system. The left side of Fig. 11.6 shows the relative phases $\varphi_s(t)$ for simulated damage in k_1 . The state of system in the baseline stage ($s = 1$) is compared with three simulated damage cases ($s = 0.75, 0.5, 0.25$) in this figure. The phase lags between DOF 2 and DOF 1 due to increasingly softened springs are clearly evident. The right side of Fig. 11.6 shows the relative phases for simulated damage in k_2 . The relative phases between DOF 2 and DOF 1 remain constant for all four cases because the damage occurring in k_2 (between DOF 3 and DOF 2) does not affect the incident energy between DOF 2 and DOF 1 for the dereverberated response.

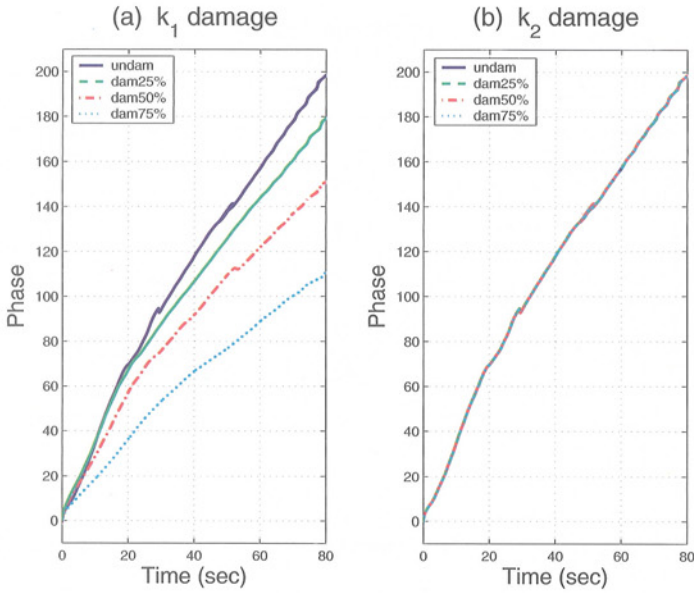


Figure 11.6: Relative phases of dereverberated response between DOF 2 and 1. (a) damage occurred in k_1 , (b) damage occurred in k_2 .

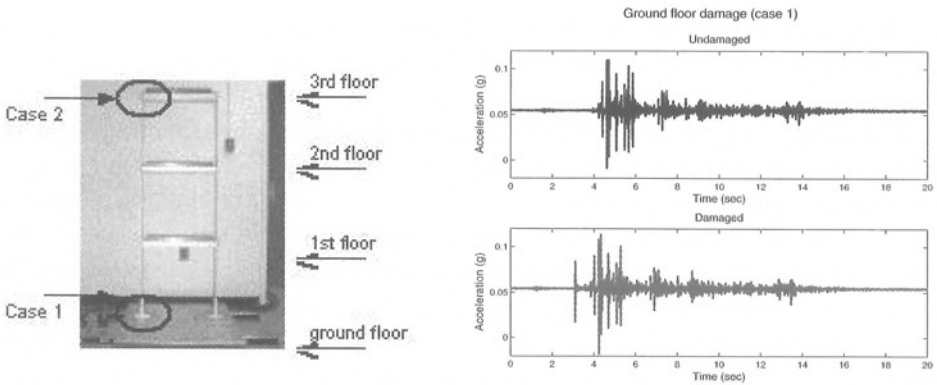


Figure 11.7: (a, left) Scaled building model and (b, right) measured acceleration time series data (in the unit of g) for undamaged and damaged ground floor response.

The use of the EMD method to obtain IMF's is essential to define and compute instantaneous phases, even for the simplest system response such as that shown in this subsection. Without employing the EMD method, the necessary property of proper rotation defined in the previous subsection cannot be guaranteed.

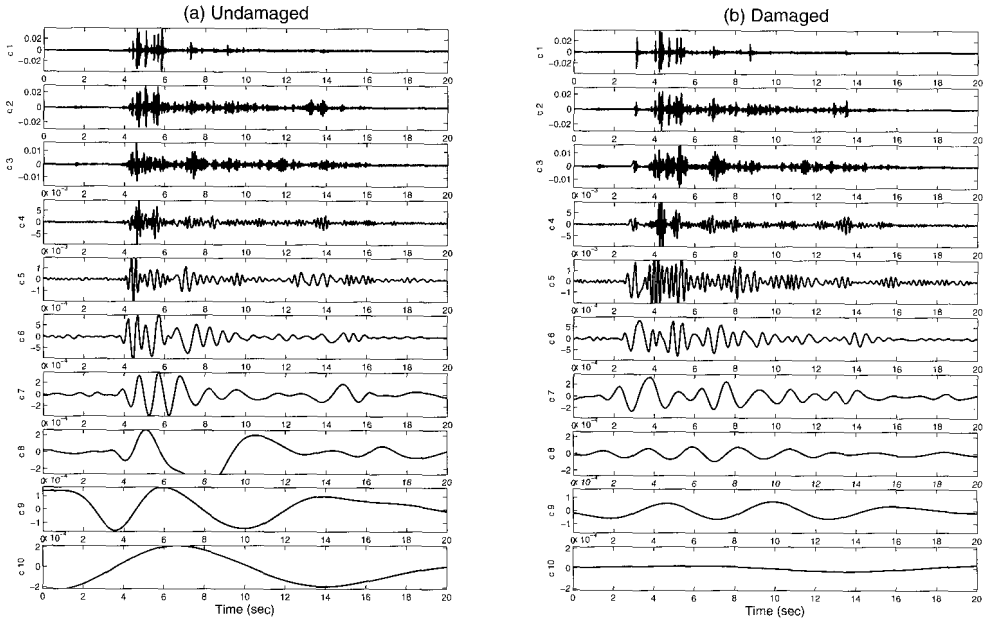


Figure 11.8: IMF components for (a) undamaged and (b) damaged response data (in units of g).

11.3.2. Experimental validations

To develop a better physical understanding of the method, a laboratory test of a scaled building model, with and without damage, is used to validate our numerical results. The building model, shown in Fig. 11.7a consists of four floors, with the ground floor driven by a hydraulic shake system. On each floor, PCB accelerometers are mounted to measure the vibratory response of the building before and after damage. To simulate seismic loading, a time series from the El Centro earthquake was used as input to the hydraulic actuators. The identified undamaged natural frequencies were determined to be 2.5, 7, and 12 Hz, respectively, for the first three modes of the structure. Two damage cases were simulated by physically changing the properties of the structure. In this study, stiffness damage was simulated by removing two bolts in the bottom flange near the ground level (Case 1), and by removing two bolts from the top floor connection (Case 2). An example of the measured response time series data, undamaged and damaged, for Case 1 of the ground floor is shown in Fig. 11.7b. These measured acceleration time series are first decomposed into sets of IMFs, and examples of IMFs are given in Fig. 11.8. Each IMF component can be viewed as an adaptive basis function derived directly from measured data. These basis functions are both amplitude- and frequency-modulated signals, and they reveal unique time-frequency features through HHT.

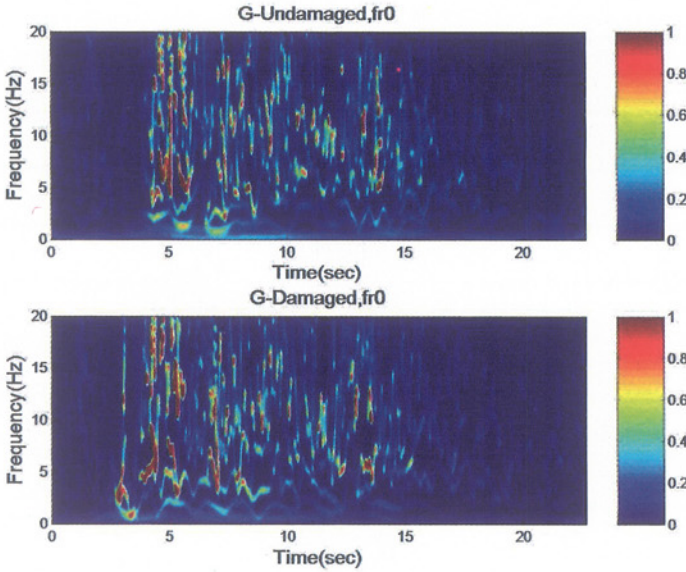


Figure 11.9: HHT spectrum of ground floor acceleration response for undamaged (top) and damaged (bottom) cases.

Figure 11.9 displays the comparison of the HHT spectrum of undamaged (top) and damaged (bottom) ground-floor response as joint functions of time (horizontal axes) and frequency (vertical axes). The spectra amplitudes are displayed as scaled images, and their normalized values are indicated by the color bars on the right side of each image. The time-frequency characteristics of the top and bottom plots, due to the richness of the structural response at the ground level, are similar, with the exception of the appearance of a noticeable distribution of broadband signal energy at about 3 s in the damage case. This feature is due mainly to the loosening of the bolts of the ground floor brace used to support the upper stories. As the seismic wave enters the ground floor, the brace bangs against the loose bolts and vertical legs of the structures, causing an impact to occur prior to the full seismic wave reaching the ground floor accelerometer.

As the seismic wave continues to traverse up the building, noticeable changes start to appear in the Hilbert response spectrum displayed in Fig. 11.10. Notice the significant loss in intensity between the undamaged and damaged responses. This loss is particularly clear if one tracks the third modal frequency band of energy between the damaged and undamaged spectra.

As the intensity in this frequency band diminishes, a new phenomenon becomes apparent in the time frequency response. At approximately 12 s, the third mode band starts to spread as the intensity decreases, suggesting the presence of a structural nonlinearity in the system caused by the loosening of the two bolts. Additional analysis by extracting the damping loss factors (Salvino 2000; Pines and Salvino

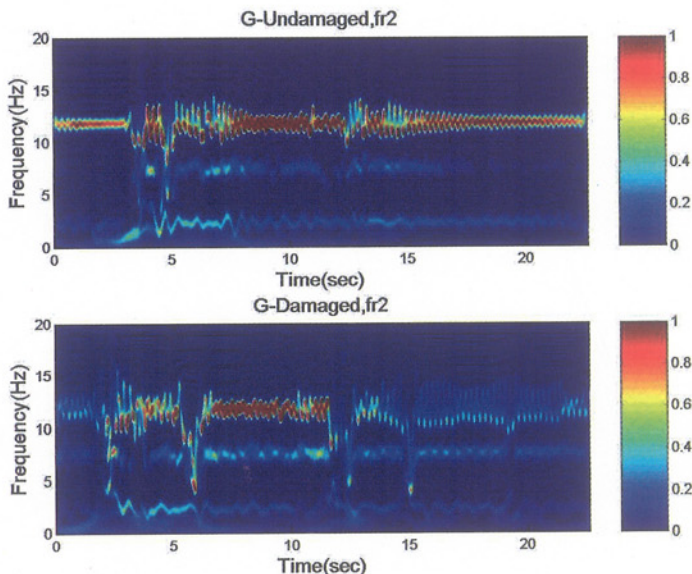


Figure 11.10: HHT spectrum of second floor acceleration response for undamaged (top) and damaged (bottom) measurements.

2002) confirms that this drop in intensity is consistent with an increase in damping in the system as a result of members sliding back and forth against one another.

Since the nonlinear/inelastic behavior of a damaged structure should be expected to affect the frequency composition of the structural response, and the novel technique of EMD and HHT spectrum is known to offer superb temporal and frequency resolution compared to that of more conventional wavelet and windowed FFT analysis methods, it is not surprising that damage in structures can be identified by using this method. Others have also studied EMD and HHT applications in system identification and damage detection for civil structural applications (Yang et al. 2004a, 2004b).

This result is particularly important when the examination of the signals recorded during a damaging event requires consideration of nonlinear behavior. These time-frequency changes must be linked to physical parameters; in other words, changes identified from response characteristics must be linked to changes in the physical properties due to damage. This problem is extremely difficult because the mathematical model never captures the true complexity of the real system. No well-established solution is available at present.

In the next subsection, we demonstrate a promising step to link the time-frequency features identified by using the empirical mode analysis to the concept of damage identification by using phase dereverberation, a concept derived from the wave mechanics for the above building model.

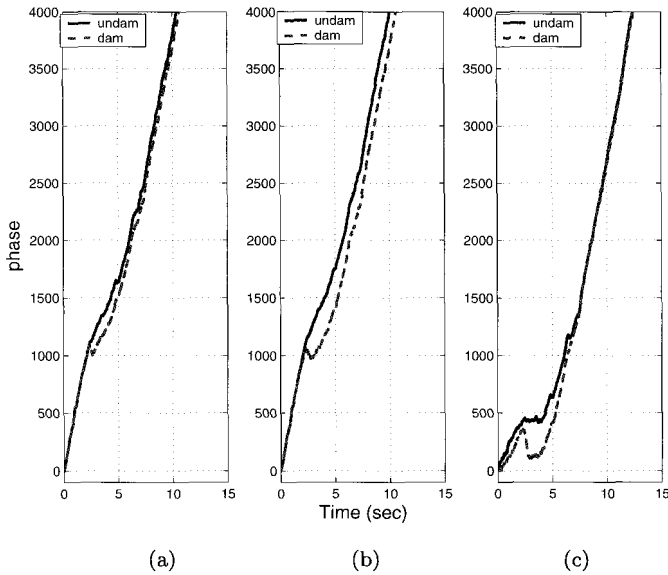


Figure 11.11: Relative phases of measured response for ground floor damage of a scaled building.

11.3.3. Instantaneous phase detection

The IMF functions such as those given in Fig. 11.8 are then used in (11.9) and (11.10) to directly obtain the phase lags as functions of time.

Figure 11.11 shows the relative phases defined in (11.10) for the undamaged baseline and the ground-floor damage case. Figure 11.11a is obtained from data on the first floor, Fig. 11.11b is from the second floor, and Fig. 11.11c is from the third floor. All sets of data use the reference point of the ground floor measurement data.

The phase lag due to damage shows up in the measured signal for each floor. These phase lags can be directly attributed to the stiffness loss of the structure based on the numerical study given in subsection 11.3.1. In addition, the locations of the measurements clearly indicate that the damage must have occurred between the ground and first floors since the magnitude of the phase lags are proportional as the seismic wave continues traveling from the ground floor to the top floor.

Figure 11.12 shows the top floor damage case where the relative phases were computed in the same way as those for Fig. 11.11. The phase lag due to damage shows up in the measured signal of the top floor only, indicating the structural damage is located between the top two accelerometers or between the second and third floors.

To further demonstrate the concept of combining an instantaneous phase of a measured structural response with the values of the physical parameters of a structure, a linear approximation of a one-dimensional asymmetric structural element was studied analytically. The results can be found in Pines and Salvino (2004). The

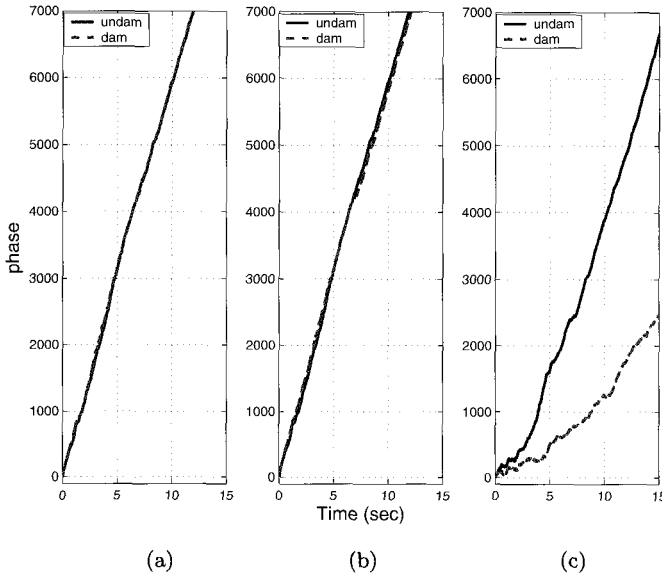


Figure 11.12: Relative phases of measured response for top-floor damage of a scaled building.

phase delay, which is expressed by physical quantities such as mass and stiffness in the closed-form solutions of linear approximation, is identical to the phase functions given in (11.3)–(11.5) below the cutoff frequency.

The basic concept of a new structural-damage-detection method is presented in this subsection. This method tracks the changes in wave speed through each individual structural element between successive degrees of freedom. The examples given, both the simple numerical simulation and the experimental results, have shown that the method can be an effective technique for identifying and locating damage. Quantifying the amount of structural damage present in the structure requires correlating these relative phases with the known values of stiffness between each degree of freedom. The procedure is similar to that of previous work (Ma and Pines 2003).

11.4. Frame structure with multiple damage

The EMD and HHT technique in conjunction with a wave-mechanics based structural health monitoring method has been presented in the previous subsection for a one-dimensional structure. Here, in this subsection, this approach is extended through experimental demonstrations to a more generalized structure with damage in multiple locations. Furthermore, the instantaneous phase detection method is compared with a more conventional time-domain approach using an auto-regressive modeling technique as well as another recently proposed damage-detection method using geometric properties of deterministic dynamics. These comparative studies

Table 11.1: Damage case summary description.

Damage Case	Damage Location
0 (baseline)	All bolts at 12.4 N-m (110 in-lbf) torque
1	Joint D bolts removed
2	Joint A bolts removed
3	Joint B bolts removed
4	Joints A and D bolts removed
5	Joints A, B, and D bolts removed

show the wide applicability and adaptive nature of the instantaneous phase detections approach. In addition, direct comparisons of these three methodologies provide the reader with examples of the rapidly evolving SHM approach, which is based on data-driven or empirical modeling techniques.

11.4.1. *Frame experiment*

A scaled three-story frame structure was used to perform the experimental demonstration. A photograph of the test structure is shown on the left side of Fig. 11.13. The floors were 1.3-cm-thick (0.5-in-thick) aluminum plates with two bolt connections to brackets on the aluminum unistrut columns. The base was a 3.8-cm-thick (1.5-in-thick) aluminum plate. Support brackets for the columns were bolted to this plate. Further details of this structure may be found in Fasel et al. (2002). Damage was created by removing the bolts for various combinations of the connections between floor 1 and the three unistruts (right side of Fig. 11.13). The baseline condition (undamaged) and five damage scenarios are summarized in Table 11.1.

An electromechanical shaker was connected to the structure at the mid-height of the base plate so that translational motion could be imparted. The structure was instrumented with six piezoelectric accelerometers on floor 1 only. Accelerometers were mounted on blocks glued to three of the unistrut columns (joints A, B and D) at the floor level, in both in-plane directions. Additionally, a force transducer was mounted between the stinger and the base plate and used to measure the input to the base of the structure. A commercial-data acquisition system controlled from a laptop PC was used to digitize the accelerometer and force transducer analog signals.

Two methods of interrogation were used to excite the structure in order to perform the comparative studies mentioned previously. The excitation signals include both a deterministic chaotic input source and a random white noise input source. The chaotic excitation signal was generated by the well-known Lorenz oscillator explicitly given by the vector $\mathbf{y}(t) = [y_1, y_2, y_3]$ in (11.6).

A simple input/output MATLAB SIMULINK™ model along with XPC Target™ and a commercially available signal conditioner was used to send the

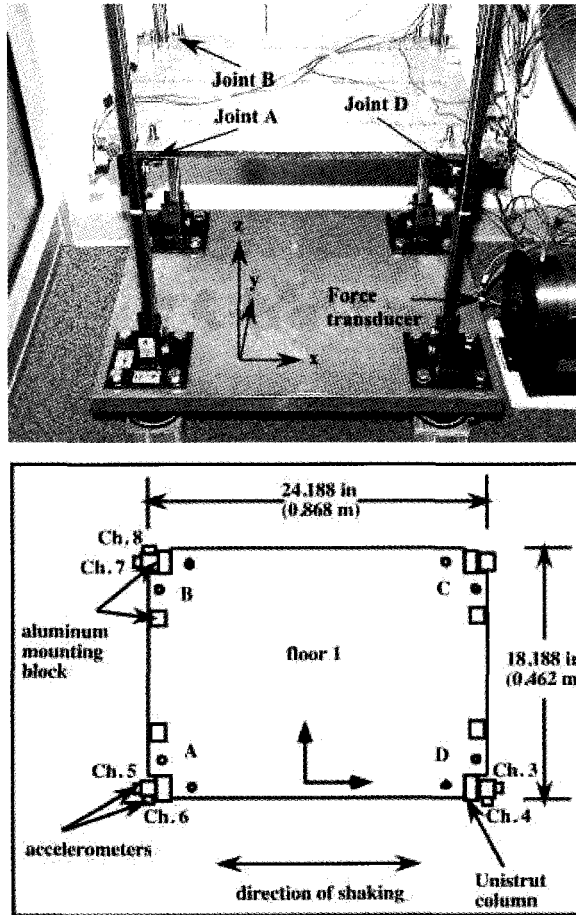


Figure 11.13: Frame experimental set-up showing instrumented floor at joints A, B, and D.

pre-digitized chaotic Lorenz waveform to the shaker. The waveform was sent at a 5000 Hz shaker update rate, and the analog sensors were sampled at 1500 Hz with $N_t = 16384$ total sample points. Five sets of baseline undamaged datasets were recorded before damage was introduced to the structure. Similarly, the test procedure was repeated for each of the damage cases, resulting in $N_r = 5$ runs at each of $N_d = 6$ total damage cases (including the baseline) to give 30 total datasets. The sample shaker input (channel 1), force transducer response (channel 2), and acceleration response signals (channel 3 and channel 4) are shown in Fig. 11.14, along with their corresponding phase portraits generated by delay coordinate constructions (Kantz and Schreiber 1999).

The driving signal and the force felt by the structure closely track the input Lorenz waveform, Figs. 11.14a and 11.14b, with some differences in the latter primarily due to structural feedback. The response acceleration time series, however,

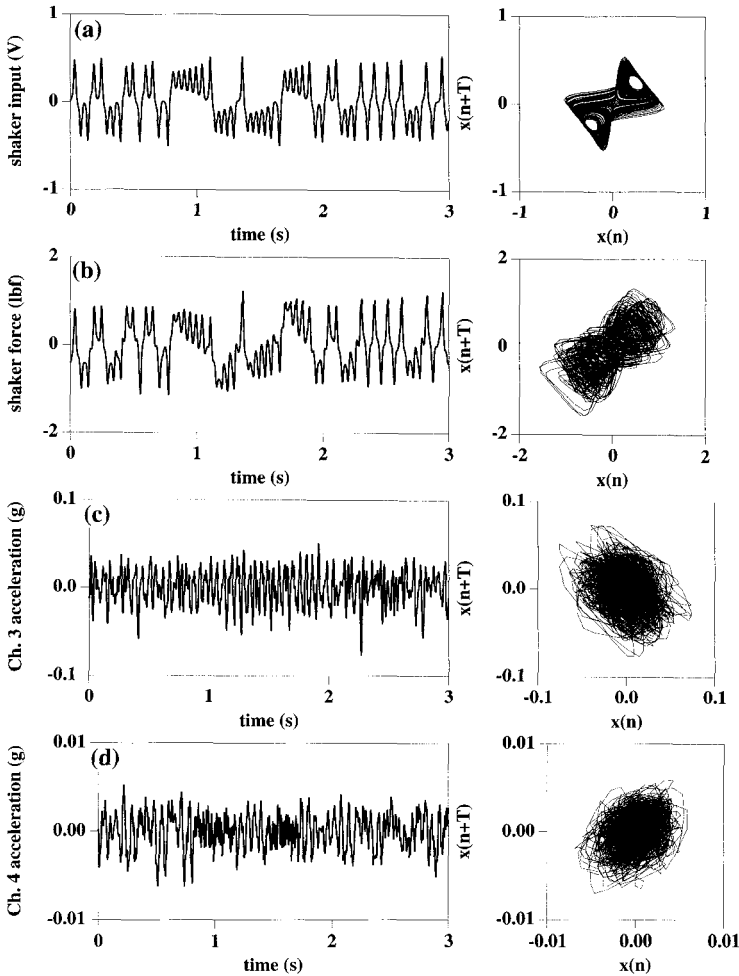


Figure 11.14: Typical 3-s time windows (left column) and their delay coordinate constructions (right column) for (a) raw voltage input to shaker, (b) force transducer output (channel 2), (c) channel 3 acceleration, and (d) channel 4 acceleration.

are less clearly “structured” and illustrate the filtering effect of the structure on the input signal. Both co-directional (channel 3 in Fig. 11.14c is in the same direction as the excitation) and contra-directional (channel 4 in Fig. 11.14d is perpendicular to the direction of excitation) sensor data are shown in order to highlight the differences in response data from these two directions. Although the damage identification analyses were performed for many different locations on the frame, or, in other words, all channels of measured data were studied, we show the results only for channel 3 data in subsections 11.4.2–11.4.5, providing direct comparisons of three entirely different data-driven SHM methods.

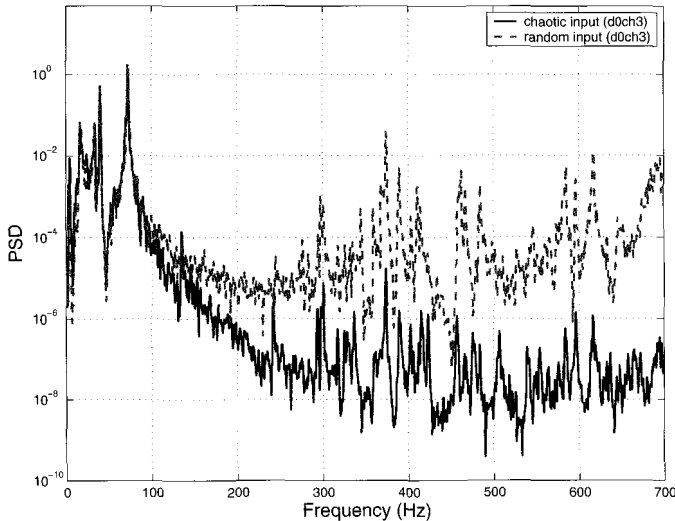


Figure 11.15: Power spectral density of channel 3 data for baseline frame excited by chaotic input and excited by random input.

Additionally, broadband random signals were also applied to excite the frame. The test procedure was repeated for the baseline and for each of the damage cases. The data were sampled under the same conditions as those of the chaotic input except $N_t = 8192$ total sample points were recorded for each of the 30 datasets. Examples of the power spectral density (PSD) obtained from the baseline structural response measurement (channel 3 time series) are given in Fig. 11.15.

The characteristic comparisons displayed on the PSD plot for chaotic and random forcing indicate that distinct structural response differences occur in the energy distributions. Even though the fundamental structural modes being excited are somewhat similar for the lower frequencies, the floor level of the higher frequency region is much lower for the chaotic driving condition. This finding may indicate a high signal-to-noise ratio or more clean structural-response data. We must point out that although the Lorenz oscillator's input appears fairly complex in the time domain, its dynamics in phase space is low-dimensional. The power spectra density cannot reveal its unique chaotic dynamic nature.

11.4.2. Detecting damage by using the HHT spectrum

The time series from the frame experiment described in subsection 11.4.1 were analyzed initially by using the EMD and HHT method. The first step in this procedure is to decompose the data into a set of IMF functions; in other words, the measured time series is represented by a sum of n amplitude- and frequency-modulated functions, each satisfying the condition of monotonically increasing phase and positive frequency. This step, as stated in a previous subsection, is the fundamental aspect

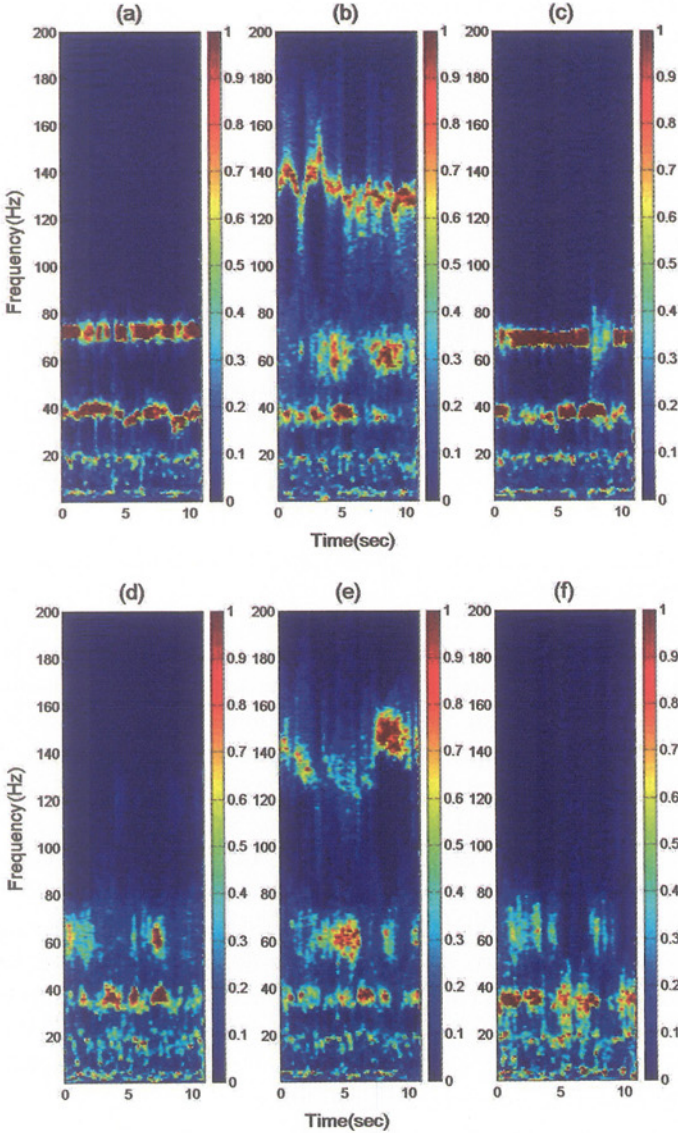


Figure 11.16: Hilbert spectra for baseline and different cases of frame damage.

of the method. These IMF functions are then used to compute the Hilbert transform and to construct the HHT, $H(f, t)$. Figure 11.16 displays the the comparison of the HHT for the channel 3 data of the baseline (Fig. 11.16a) and damage cases 1–5 (Figs. 11.16b–f, respectively) given in Table 11.1.

Figure 11.16 provides a good initial visual comparison of the structural response as joint functions of time (horizontal axes) and frequency (vertical axes). As in

Figs. 11.9 and 11.10, the spectra amplitudes are displayed as scaled images, and their normalized values are indicated by the color bars on the right side of each image. Many features in $H(f, t)$ can be interpreted to explain the frame behavior for each damage case. Generally, many more temporal features are noticeable when the structure becomes damaged. The damaged frame exhibits different degrees of frequency lowering, widening, and intensity loss. This finding suggests the presence of a structural nonlinearity in the system caused by stiffness loss at the joints. For example, the baseline frame (Fig. 11.16a) is quite different compared to each of the damaged cases at approximately 40 Hz. Note that the channel 3 measurements displayed in Fig. 11.16a–f are the accelerometer outputs closest to the driving location and to joint D. The frequency band between 140–160 Hz that is clearly present in Figs. 11.16b and 11.16e but not in the others appears to be due to the damage caused by removing bolts at joint D (damage cases 1 and 4 in Table 11.1).

The Hilbert spectra analysis can be beneficial for understanding the overall frame behavior resulting from each of the damage cases. However, the relative phase relationship introduced in the previous subsections can provide further understanding of the time-frequency changes in terms of physical parameters. Natural connections can be made from the changes identified through the response characteristics to changes in the physical properties due to damage.

11.4.3. Detecting damage by using instantaneous phase features

In this subsection, the damage identification for the frame structure is based on the comparison of the relative phase values of frame vibratory response before and after damage. As explained previously, when damage in a structure is present, this damage will alter the speed at which energy traverses through the structure. For the baseline undamaged frame $s = 0$, variable $\varphi_s(t)$ given in (11.10) is calculated by using the measured acceleration signal. The result is then compared with the $\varphi_s(t)$ values obtained by using the acceleration data at the same locations for a variety of different damage cases $s = 1, 2, 3, 4, 5$. Figure 11.17 displays examples of comparing $\varphi_0(t)$ (baseline) and $\varphi_1(t)$ (damage case 1 — Joint D bolt removed).

The vertical axis is given by unwrapping radian phases with changing absolute jumps greater than π to their 2π complement, just as we did in the figures of the instantaneous phase. The two curves in Fig. 11.17 provide a comparison of $\varphi_1(t)$ and $\varphi_0(t)$, where $s = 0$ indicates the baseline frame, and $s = 1$ indicates the damage case 1 (joint D damage in this example). Channel 3 data for the baseline frame and for the frame with damage case 1 are used to calculate $\theta_p(t)$. Channel 2 data are used to calculate $\theta_0(t)$.

Figure 11.17 clearly illustrates the changes of the phase relationships relative to the driving point due to the presence of damage in the system. The reference point used here is chosen to be the excitation force measurement point (channel 2). This choice of the reference phase function $\theta_0(t)$ gives larger values compared with $\theta_p(t)$, for all t , for both undamaged and damaged cases. Because of this choice for

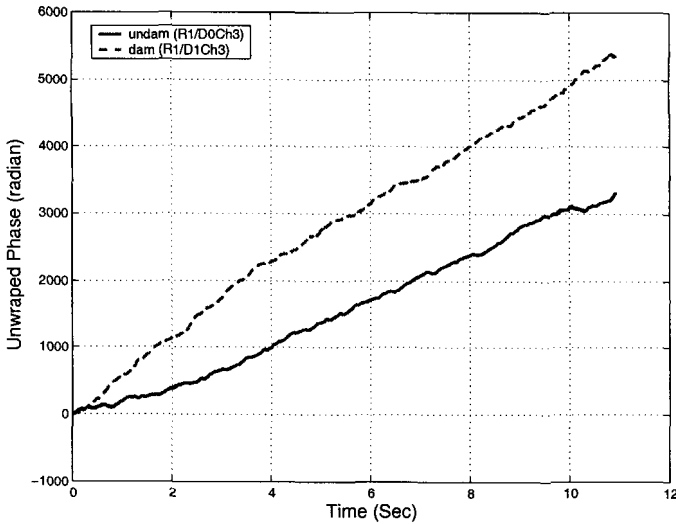


Figure 11.17: Variable $\varphi_0(t)$ for baseline frame is compared with $\varphi_1(t)$, frame with damage case 1 (joint D damage).

$\theta_0(t)$, the phase difference $\theta_p(t) - \theta_0(t)$ will be negative for all t , again for both the damaged and undamaged cases. However, the relative phase $\varphi_s(t)$ defined in (11.10) is the absolute value of the phase difference. The curve for the damaged case lies above the curve for the undamaged case in Fig. 11.17 because of the choice for $\theta_0(t)$ and the use of the absolute value in the definition (11.10).

The choice of a reference point (channel 2) is based purely on considerations of the signal-to-noise ratio and the measurement quality. When the reference points on a structure are varied, such as by using channel 5 and channel 7 data to calculate $\theta_0(t)$, damage can be located based on the geometry of the structure. More systematic research will be conducted on this topic in the future.

To measure the average phase change between the baseline and the damaged structure, a mean phase error is introduced as a feature value or damage index:

$$E = \sqrt{\frac{\sum_{t=1}^{N_t} [\varphi_1(t) - \varphi_0(t)]^2}{\sum_{t=1}^{N_t} \varphi_0^2(t)}}. \quad (11.17)$$

The feature values can be computed for all $N_r = 5$ runs of each of the $N_d = 6$ total damage cases (including the baseline). The results for the channel 3 data are shown in Fig. 11.18.

The E value provides an average phase difference measured between two locations on a structure for two different structural conditions such as the baseline and damaged frame. In other words, the E value indicates the average deviation for the phases of a structural wave from its baseline state. A greater E value shows larger

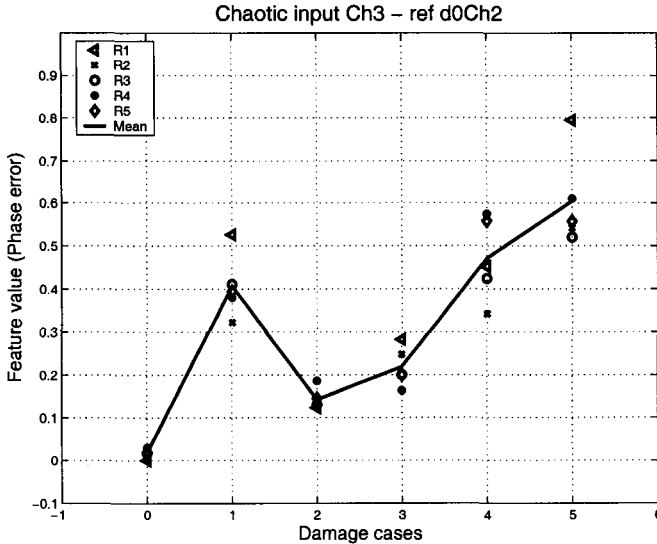


Figure 11.18: Damage index (feature value) calculated from channel 3 data for all five runs of each of the 6 total damage cases including the baseline case.

phase differences and may indicate more severe damage or a larger alteration from the baseline state. The phase error E value for the baseline frame (damage case=0) was calculated by using the channel 3 data from all 5 runs to obtain $\theta_p(t)$ and channel 2 data from the first run (R1) to obtain $\theta_0(t)$. As a result, $\theta_p(t)$ calculated by using the first run (R1) gives an identically zero E value as expected. However, the E values calculated from runs 2 to 5 (R2-R5) provide a good range of statistical error. As can be seen, all the E values for the baseline case are at least an order of magnitude smaller than the E values for any of the damaged cases.

The feature E value displayed in Fig. 11.18 discriminates among all damage cases except between cases 1 and 4. Channel 3, as indicated in Fig. 11.13, is located at joint D and provides overwhelmingly strong signatures for case 1 damage (bolts removed at joint D). Better discrimination can be expected between damage cases 1 and 4 when data from other channels are used. Similar analyses were performed for other measurement channels, and the results were consistent with those for channel 3.

As mentioned previously, broadband random signals are also applied to excite the frame. The frame response magnitudes are in the same range as those for the chaotic excitations. The output response time series from random forcing are also used to calculate the feature E value. Direct comparisons of random and chaotic excitation E values for the channel 3 data can be found in Salvino et al. (2003). Although the averaged E follows somewhat the same trend compared to that of the chaotic excitation cases, large fluctuations are observed between different runs. The use of broadband forcing present a much greater challenge as far as signal process-

ing is concerned. Improved E values can be obtained when the data are filtered. The improvement and the final results critically depend on the characteristics of the filter used. Obviously, this approach is not desirable either for gaining a basic understanding of the physics involved or for practical application and implementation. A more conventional modeling technique that lends itself to stochastic excitations is presented below in subsection 11.4.4.

11.4.4. *Auto-regressive modeling and prediction error*

A pure time-domain approach for empirical modeling of time series data is autoregressive (AR) modeling. Here, the future system output is approximated by regressions of the past values of the dynamics. This approach is also data-driven in that all parameters are estimated from the response signal alone. The only assumption is that the output is a linear combination of the past values, such that the underlying equation of the AR model is given by

$$x(n) = a_0 + \sum_{j=1}^{\beta} a_j x(n-j) + \eta_n, \quad n = 1, 2, \dots, N. \quad (11.18)$$

The $x(n)$ are observed measurements, and the a_j values denote the AR regression coefficients, and the η_n are taken as Gaussian white noise. Therefore, (11.18) is most appropriately used for the modeling of linear stochastic processes. Coefficients for the AR model are computed by solving the over-determined least-squares problem

$$\begin{bmatrix} x(\beta+1) \\ x(\beta+2) \\ \vdots \\ x(\beta+N) \end{bmatrix} = \begin{bmatrix} 1 & x(\beta) & x(\beta-1) & \cdots & x(1) \\ 1 & x(\beta+1) & x(\beta) & \cdots & x(2) \\ \vdots & \vdots & & \ddots & \\ 1 & x(N-1) & \cdots & \cdots & x(N-\beta) \end{bmatrix} \begin{bmatrix} a_0 \\ a_1 \\ \vdots \\ a_\beta \end{bmatrix}. \quad (11.19)$$

The order of the model is denoted by β and defines the number of past observations used in determining the present value. Numerous methods for choosing an appropriate model order appear in the literature. The model order should be at least as large as the number of frequencies one hopes to capture, for roots of the polynomial defined by the coefficients give the poles of the system's rational transfer function (Owen et al. 2001). While a certain minimal number of past values are necessary to accurately predict any future values, too many parameters can lead to overfitting. Overfitting occurs when the peculiarities of the actual signal, such as noise and intrinsic fluctuations, are interpreted as global features of the system (Kantz and Schreiber 1999).

The autocorrelation function of the data is often a good indicator for choosing an appropriate order. Fast decay rates of the autocorrelation function imply that the time series has a "short memory"; hence, a lower order model is appropriate. Probably the most common approach is to form a cost function for the selection of β that involves a "goodness of fit" term and a penalty term for a high model

order. One such example is the final prediction error (FPE) criteria given by Akaike (1969) and Owen et al. (2001). For health-monitoring applications, the importance of model order is somewhat diminished. The goal in SHM is not necessarily to make accurate forecasts, but to construct a model that breaks down in the presence of damage.

In this subsection, the idea is to use the time series taken from the “pristine” structure to reconstruct a reference, or baseline, system AR model. This AR model is then used to forecast or predict the system’s response by using data taken at later times, when the structure may possibly have been damaged. Such an approach falls within the context of supervised learning where data from known particular damage cases must be obtained for later classification purposes. The working hypothesis is that damage accumulation will alter the structure’s dynamic response, causing these baseline models to lose their ability to make predictions. The error formed between prediction and actual measurement, called the *prediction error*, is proposed as a good candidate feature for quantifying both the presence and magnitude of structural degradation.

A group of N_r time series measurements $x_i(n), i = 1, \dots, N_r$, from a given sensor location are taken from the structural vibration response (subject to random Gaussian excitation). Recording N_r such independent responses allows for the inclusion of ambient variation in the set of baseline data. Such variation is known to occur in practice and must be accounted for if damage-induced changes are to be distinguished from those due to environmental factors. The AR coefficients are determined for each of these reference datasets. The coefficients are then used to create forecasts on a subsequently measured time series $y_i(n)$. For a given time series, the future value \hat{y} of a randomly chosen fiducial point $y(f)$ is predicted by using the model generated with the baseline data $x(n)$ as

$$\hat{y}(f+1) = a_0 + \sum_{j=1}^{\beta} a_j y(f-j+1), \quad (11.20)$$

shown here for prediction horizon $s = 1$. Subsequent predictions for $s > 1$ may be made by incorporating the predicted values into (11.20) in order to make continued forecasts. The residual errors between the actual and predicted values are the damage-sensitive feature, computed at the fiducial point f by

$$\gamma_f = |\hat{y}(f+s) - y(f+s)| / \sigma_x^2, \quad (11.21)$$

where the metric has been normalized by the variance of the reference signal, σ_x^2 . This metric tests the ability of a model derived from one set of data [in this case, the a_j computed from the $x(n)$] to make predictions on the other time-series $y(n)$. This process is applied to each of the N_r^2 possible pairs of time-series and for some number of fiducial points to generate a distribution of feature values .

This procedure was applied to the channel 3 sensor data of the test structure described previously. The excitation signal was taken to be broadband, Gaussian

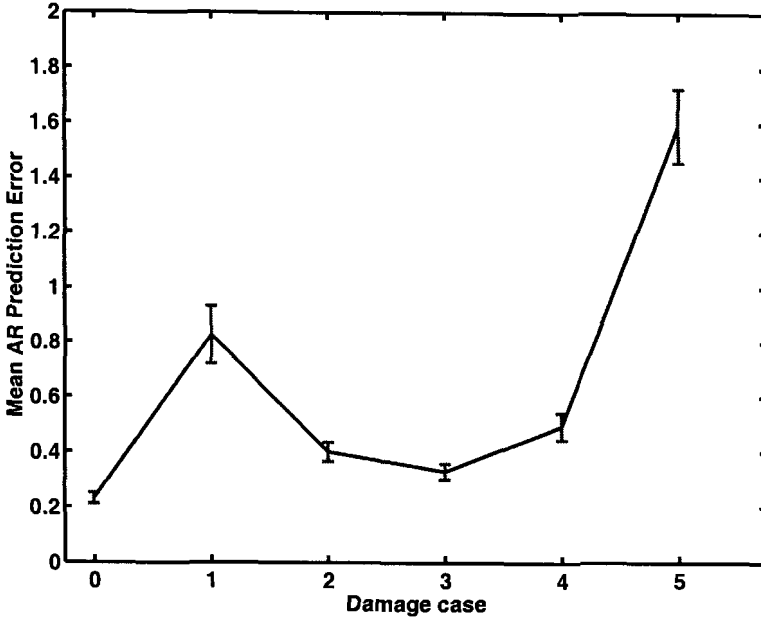


Figure 11.19: AR mean prediction error as a function of damage cases.

noise in accordance with (11.18). Each time series (for all damage levels) was first normalized by subtracting the mean and dividing by the standard deviation. The structure's response for the undamaged scenario was then used to build an AR model by solving (11.19) with model order $\beta = 5$ (based on the autocorrelation structure of the baseline time series). Subsequent data from the damaged structure were then tested against this model by means of (11.20) and the prediction error γ recorded for $f = 1, 2, \dots, 5000$ randomly chosen fiducial points.

The probability density functions (PDFs) associated with the prediction errors for each damage case were first computed, and, as expected, the distributions appeared Gaussian. The mean values from these distributions along with 95% data quantiles for AR model prediction error plotted as a function of the damage cases are shown in Fig. 11.19. Not surprisingly, damage scenarios 1 and 5 show up clearly as they both involved the removal of the bolts at joint D (the location of channel 3). Other damage scenarios show less deviation from the baseline. The PDFs of the prediction errors also show that larger damage results in a larger variance associated with the prediction. As the baseline model breaks down, not only do predictions become less accurate, but the errors have a much wider spread. This result is consistent with those of previous observations using prediction error metrics in SHM.

This simple implementation of an AR approach is effective in diagnosing damage-induced changes to the dynamics. More complicated variants of the AR modeling can be used for SHM purposes including addition of exogenous inputs (ARX model,

see Sohn et al. 2001), addition of a moving average term to better account for noise (ARMA, ARMAX models, see Fassois 2001), and the extension to multivariate signals (see Bodeux and Golival 2003 for an ARMAV approach to SHM). Building empirical models and then searching for model breakdown as a damage indicator can be an effective method for monitoring complicated structures for which no analytical model exists.

11.4.5. Chaotic-attractor-based prediction error

Many of the time series methods used to do structural damage assessment rely upon analyzing transient dynamic or stochastic time series, e.g., on using modal analysis (the modal method) or the AR modeling discussed in the previous subsection. Nichols et al. (2003a,b) and Todd et al. (2001) have proposed assessing the steady-state dynamics imposed by a deterministic waveform. Specifically, these authors used a chaotic waveform to excite a structure and then developed methods for comparing the resulting attractors obtained as the structure became damaged over time.

A variety of metrics exist for detecting differences in dynamical attractors. Much work has focused on using the correlation dimension (see Logan and Mathew 1996; Craig et al. 2000; Wang et al. 2001), although this method's numerous important shortcomings and pitfalls were discussed in Nichols (2003c). In a supervised learning context similar to that described in the last subsection, the idea is to use data taken from the "pristine" structure to reconstruct reference, or baseline, attractors. These data are to be compared to the data collected from the structure at subsequent times, when damage may or may not have occurred to the structure. By using a simple attractor geometry prediction scheme, points on the "damaged" attractors are forecast by using the baseline data as a model. Similarly to how the errors is used in the AR approach, the error formed between prediction and measurement is used here to detect and quantify damage-induced changes in the dynamics. The models make no assumptions about the underlying system, in contrast to the models used in AR modeling techniques, which implicitly assume a response coming from a structure for which a linear model is an accurate descriptor.

As with the AR approach, the method begins by recording a set of N_r baseline time series when the structure is in its baseline condition. This baseline set of experiments is represented by $X = \{x_1(n), x_2(n), \dots, x_{N_r}(n)\}$, where each $x_u(n)$, $u = 1, 2, \dots, N_r$, is a vector of discretely sampled values of structural response time series consisting of $n = 1, 2, \dots, N$ points. The discrete time index n refers to the value recorded at sample time $t_s = n\Delta t$, where $1/\Delta t$ is the sampling frequency. New "test" data are collected at some later time from the same location on the structure, denoted by $Y = \{y_1(n), y_2(n), \dots, y_{N_r}(n)\}$, in the same fashion that the set X was created. The next step is to use the baseline data X to empirically generate attractor-based models of the baseline structure's dynamics and observe the degree to which they predict the dynamics of subsequent "test" datasets.

The algorithm used here is adopted from Schreiber (1997), where it was used to detect non-stationarity in time-series data. A simple attractor-based prediction scheme is used on the undamaged data to forecast the values of the damaged data some number of time steps s into the future. First, each of the baseline time series in X and Y are used to reconstruct attractors in phase space by using the embedding theorems (Takens 1981; Sauer et al. 1991). The method proceeds by comparing any of the baseline attractors to any of the “test” attractors in the following way: given a randomly selected trajectory with time index f on a reconstructed “test” attractor $\mathbf{y}(f)$, the algorithm selects the set of points on the baseline attractor $\mathbf{x}(n)$ that are within some radius ε of that trajectory

$$U_\varepsilon^{\mathbf{x}(p)}\mathbf{y}(f) = \mathbf{x}(p) : \|\mathbf{x}(p) - \mathbf{y}(f)\| < \varepsilon, \tag{11.22}$$

where $\|\cdot\|$ denotes the Euclidean norm of a vector. No temporal relationship need exist between the indices p and f , as the set is constructed purely by geometry; in other words, the $\mathbf{x}(n)$ are selected via their Euclidean distance to the fiducial point with the time index of that point passively carried along for bookkeeping. This selection method contrasts with that of an autoregressive approach, which is based on temporal relationships. In fact, this current method may be thought of as regressing in phase space geometry, similarly to how an autoregressive approach regresses in time. The idea here is to describe the evolution of the neighborhood $U_\varepsilon^{\mathbf{x}(p)}[\mathbf{y}(f)]$ and to use this description as a predictor for how subsequent data should evolve. The predicted value for $\mathbf{y}(f)$ at s time steps into the future, denoted $\hat{\mathbf{y}}(f + s)$, becomes

$$\hat{\mathbf{y}}(f + s) = \frac{1}{|U_\varepsilon^{\mathbf{x}(p)}\mathbf{y}(f)|} \sum_{\mathbf{x}(p) \in U_\varepsilon^{\mathbf{x}(p)}\mathbf{y}(f)} \mathbf{x}(p + s), \tag{11.23}$$

where the quantity $|U_\varepsilon^{\mathbf{x}(p)}(\mathbf{y}(f))|$ denotes the number of points in the neighborhood. The predicted value is the average of the predicted values for the neighborhood. In this sense, the baseline attractors are used as “look-up” tables which contain the various patterns present in the data. The working hypothesis is that these tables will lose their ability to serve as an accurate database as the dynamics are altered by damage. The prediction horizon s will depend on the rate at which the data are acquired and the specific application. For health-monitoring purposes, $s = 1$ will suffice if the data is reasonably sampled. While more complicated prediction schemes exist, this model is among the simplest ones that can be used to quantify the evolution of the dynamics. Because simple attractor discrimination is the objective, the absolute quality of the predictions is of diminished importance, and the simplest, most computationally efficient scheme is considered optimal. Variations of this algorithm have been used for prediction and data cleansing (see Kantz and Schreiber 1999; Nichols and Nichols 2001).

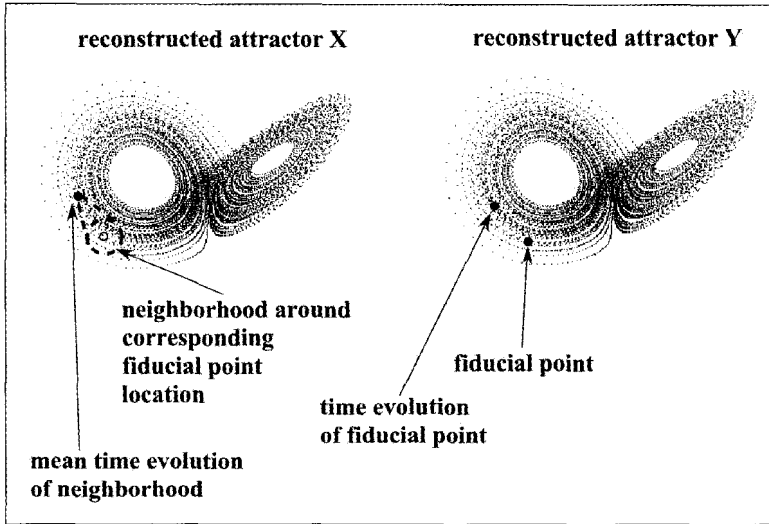


Figure 11.20: A schematic of attractor-based prediction error.

Once the predictions has been made, the s -step prediction error for trajectory f is quantified by

$$\gamma = \frac{1}{N} \sum_{j=1}^N \|\hat{\mathbf{y}}(f + s) - \mathbf{y}(f + s)\| / \sigma_x^2, \quad (11.24)$$

where σ_x^2 is again the baseline variance. Because the forecast is made in multi-dimensional phase space, the Euclidean norm is used to resolve the error to a single component. Equation (11.24) is simply the multi-dimensional analogue to (11.21). This process is repeated for some randomly selected subset of the total number of points on the attractor, resulting in a vector of prediction errors for each pair of attractors under consideration. In contrast to the one-dimensional predictions made with AR modeling (i.e., a single time series at a time), this approach is multi-dimensional, incorporating information from all the degrees of freedom by using the embedding approach.

In computing this feature, the auto-prediction error must also be computed by replacing $\mathbf{y}(f)$ with $\mathbf{x}(f)$ in (11.23). The resulting γ gives some idea of the prediction error one would expect to find if the dynamics were not changing. In order to make these “auto-comparisons,” duplicate pairings must be eliminated. For example, comparing \mathbf{x}_1 and \mathbf{x}_2 , for example, followed by comparing \mathbf{x}_2 and \mathbf{x}_1 could potentially bias the data, so such a pairing is disregarded in the second comparison. Although comparisons between data from different damage scenarios do not suffer this effect (each baseline attractor \mathbf{x} could be used to predict each test attractor \mathbf{y}) the constraint is maintained across all cross-predictions for consistency. A schematic of this algorithm is shown in Fig. 11.20.

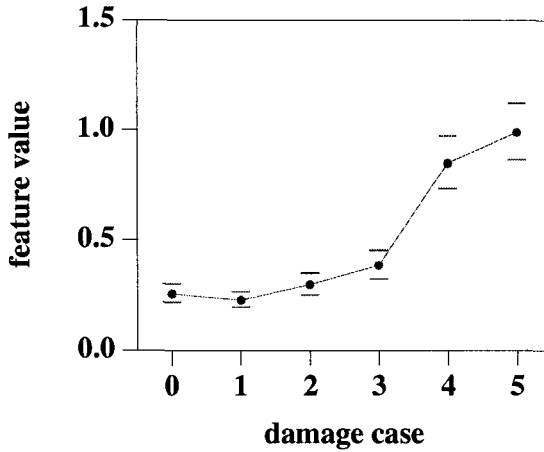


Figure 11.21: Chaotic attractor-based prediction error as a function damage cases.

This procedure was applied to the test structure described previously by using the x -coordinate [$y_1(t)$ in (11.6)] of a chaotic Lorenz oscillator as the excitation waveform. The structural response attractors were embedded in four dimensions with a delay of five time steps. For each baseline/test attractor pair, 3276 predictions were made, resulting in 32760 total values of prediction error across the multiple runs that should include ambient variation in the environmental conditions for statistical robustness. Each of the prediction error feature sets was resampled by using the mean value from 1000-member random subsets to generate 5000 “new” feature values. The resulting estimated probability density functions for the channel 3 data, similar to those for the AR model described in the previous subsection, are also fairly Gaussian after the resampling procedure. The mean values from these distributions along with 95% data quantile limits are shown in Fig. 11.21. In general, there is a reasonable separation of the PDFs, especially at damage cases 3–5, so that the classification of data into these damage cases is possible. This possibility is further reflected in the quantile limits, which do not overlap across the baseline condition and damage cases 3, 4 and 5. However, cases 4 and 5 cannot be distinguished from each other, and other data channels or a multivariate analysis combining data from all the channels was used to increase the level of sensitivity.

11.5. Summary and conclusions

We have presented a unique methodology for assessing structural damage. This method is based on instantaneous phase functions extracted from the measured time series by using EMD and IMFs. The characteristics of the damage features are then combined with phase dereverberation, a concept derived from wave mechanics. An instantaneous phase function of the measured time series is interpreted as a wave response traversing through the structure under investigation. As a structure

becomes damaged, the nature of the wave response changes and results in phase lags between designated locations on a structure when it is compared with its baseline state. Numerical examples and experimental validation for a simple one-dimensional system with, and without, damage are used to illustrate the effectiveness of the method.

Experimental studies of a simple frame structure with multiple damage cases are also presented. A simple damage-feature value (damage index) is constructed based on the average phase lags to detect frame damage for a variety of damage states. The damage-feature value is a simple and effective index that distinguishes all the damage cases presented in section 11.4. Figures 11.18, 11.19, and 11.21, as described in subsections 11.4.3–11.4.5, are calculated by using entirely different time series analysis methods or different types of data-driven modeling techniques. The quantities used by these methods (feature values or damage indexes) to identify damage are also very different. As a result, the numerical values in the vertical axes are very dissimilar in these three figures. However, as in any data-driven approach, structural damage is identified based on comparisons of the feature-value change from its baseline state. In this sense, the results obtained in the three figures are quite similar for most of the damage cases studied. In particular, the EMD and phase-detection method's results shown in Fig. 11.18 are similar to the AR modeling results in Fig. 11.19 except for those for damage case 4. Figure 11.18 is also similar to Fig. 11.21 (chaotic prediction error) except for damage case 1.

The EMD and instantaneous phase detection method does not require predefined decomposition basis functions and does not assume linear system behavior or the type of input (transient or steady state). This method, using adaptive time-varying signals (IMFs) as basis functions, can fully accommodate the physics of a system's behavior. In particular, this method is suitable for detecting structural damage by using signals measured during extreme loading events, such as earthquakes and shocks, where the nonlinear response associated with structural damage may be important to consider.

References

- Akaike, H., 1969: Fitting autoregressive models for prediction. *Ann. Inst. Stat. Math.*, **21**, 243–249.
- Bodeux, J. B., and J. C. Golinval, 2003: Modal identification and damage detection using the data-driven stochastic subspace and ARMAV methods. *Mech. Syst. Signal Process.*, **17**, 83–89.
- Chang, F.-K., 2001: *Structural Health Monitoring 2000*. CRC Press, 1062 pp.
- Chang, F.-K., 2003: *Structural Health Monitoring 2003: From Diagnostics & Prognostics to Structural Health Management*. DEStech Publications, Inc, 1552 pp.
- Cohen, L., 1995: *Time-Frequency Analysis*. Prentice Hall, 299 pp.
- Craig, C., R. D. Neilson, and J. Penman, 2000: The use of correlation dimension in condition monitoring of systems with clearance. *J. Sound Vib.*, **231**, 1–17.

- Doebling, S. W., C. R. Farrar, M. B. Prime, and D. W. Shevitz, 1996: *Damage Identification and Health Monitoring of Structural and Mechanical Systems from Changes in Their Vibration Characteristics: A Literature Review*. Tech. Report. LA-13070-MS, Los Alamos, NM, 118 pp.
- Doebling, S. W., C. R. Farrar, M. B. Prime, and D. W. Shevitz, 1998: A review of damage identification methods that examine changes in dynamic properties. *Shock Vib. Digest*, **30**, 91–105.
- Fassois, S. D., 2001: MIMO LMS-ARMAX identification of vibrating structures—Part I: The method. *Mech. Syst. Signal Process.*, **15**, 723–735.
- Fasel, T. R., S. Gregg, T. Johnson, C. R. Farrar, and H. Sohn, 2002: Experimental modal analysis and damage detection in a simulated three story building. *Proc. IMAC XX: Conf. on Struct. Dynam.*, Los Angeles, CA, Soc. Exper. Mech., 590–595.
- Huang, N. E., Z. Shen, S. R. Long, M. C. Wu, H. H. Shih, Q. Zheng, N.-C. Yen, C. C. Tung, and H. H. Liu, 1998: The empirical mode decomposition and the Hilbert spectrum for nonlinear and non-stationary time series analysis. *Proc. R. Soc. London, Ser. A*, **454**, 903–995.
- Kantz, H., and T. Schreiber, 1999: *Nonlinear Time Series Analysis*. Cambridge University Press, 304 pp.
- Logan, D., and J. Mathew, 1996: Using the correlation dimension for vibration fault diagnosis of rolling element bearings. *Mech. Syst. Signal Process.*, **10**, 241–264.
- Ma, J., and D. J. Pines, 2003: Damage detection in a building structure model under seismic excitation using dereverberated wave mechanics. *Eng. Struct.*, **25**, 385–396.
- Nichols, J. M., and J. D. Nichols, 2001: Attractor reconstruction for nonlinear systems: A methodological note. *Math. Biosci.*, **171**, 21–32.
- Nichols, J. M., M. D. Todd, and J. R. Wait, 2003a: Using state space predictive modeling with chaotic interrogation in detecting joint preload loss in a frame structure experiment. *Smart Mater. Struct.*, **12**, 580–601.
- Nichols, J. M., M. D. Todd, M. Seaver, and L. N. Virgin, 2003b: Use of chaotic excitation and attractor property analysis in structural health monitoring. *Phys. Rev. E*, **67**, Art. No. 016209.
- Nichols, J. M., L. N. Virgin, M. D. Todd, and J. D. Nichols, 2003c: On the use of attractor dimension as a feature in structural health monitoring. *Mech. Syst. Signal Process.*, **17**, 1305–1320.
- Owen, J. S., B. J. Eccles, B. S. Choo, and M. A. Woodings, 2001: The application of auto-regressive time series modelling for the time-frequency analysis of civil engineering structures. *Eng. Struct.*, **23**, 521–536.
- Pines, D. J., and L. W., Salvino, 2002: Health monitoring of one-dimensional structures using empirical mode decomposition and the Hilbert–Huang transform. *Proc. 9th Annu. SPIE Smart Struct. Mater. Conf.*, San Diego, CA, SPIE, 127–143.

- Pines, D. J., and L. W. Salvino, 2004: Structural health monitoring using empirical mode decomposition and the Hilbert phase. *J. Sound Vibr.*, in press.
- Purekar, A. S., and D. J. Pines, 2000: Detecting damage in non-uniform beams using the dereverberated transfer function response. *Smart Mater. Struct.*, **9**, 429–444.
- Salvino, L. W., 2000: Empirical mode analysis of structural response and damping. *Proc. 18th Int. Modal Analysis Conf.*, San Antonio, TX, Soc. Exper. Mech., 503–509.
- Salvino, L. W., and D. J. Pines, 2002: Structural damage detection using empirical mode decomposition and HHT. *6th World Multi-Conf. on Systemics, Cybernetics and Informatics*, Orlando, FL, Int. Inst. Informatics Systemics (IILS), 293–298.
- Salvino, L. W., D. J. Pines, M. D. Todd, and J. M. Nichols, 2003: Signal processing and damage detection in a frame structure excited by chaotic input force. *Proc. 10th Annu. SPIE Smart Mater. and Struct. Conf.*, San Diego, CA, SPIE, Vol. 5049, 639–650.
- Sauer, T., J. A. Yorke, and M. Casdagli, 1991: Embedology. *J. Stat. Phys.*, **65**, 579–616.
- Schreiber, T., 1997: Detecting and analyzing nonstationarity in a time series using nonlinear cross predictions. *Phys. Rev. Lett.*, **78**, 843–846.
- Sohn, H., C. R. Farrar, N. F. Hunter, and K. Worden, 2001: Structural health monitoring using statistical pattern recognition techniques. *J. Dynam. Syst.*, **123**, 706–711.
- Takens, F., 1981: Detecting strange attractors in turbulence. *Dynamical Systems and Turbulence*, D. A. Rand and L. S. Young, Eds., Lecture Notes in Mathematics, Vol. 898, Springer-Verlag, 366–381.
- Todd, M. D., J. M. Nichols, L. M. Pecora, and L. N. Virgin, 2001: Vibration-based damage assessment utilizing state space geometry changes: Local attractor variance ratio. *Smart Mater. Struct.*, **10**, 1000–1008.
- Wang, W. J., J. Chen, X. K. Wu., and Z. T. Wu, 2001: The application of some non-linear methods in rotating machinery fault diagnosis. *Mech. Syst. Signal Process.*, **15**, 697–705
- Yang, J. N., Y. Lei, S. Lin, and N. Huang, 2004a: Hilbert–Huang based approach for structural damage detection. *J. Eng. Mech. Div. (Amer. Soc. Civ. Eng.)*, **130**, 85–95.
- Yang, J. N., Y. Lei, S. L. Lin, and N. Huang, 2004b: Identification of natural frequencies and damping ratios of in-situ tall buildings using ambient vibration data. *J. Eng. Mech. Div. (Amer. Soc. Civ. Eng.)*, **130**, 570–577.

Liming W. Salvino

Code 652, Carderock Division, Naval Surface Warfare Center, West Bethesda, MD 20817-5700, USA

salvinohw@nswccd.navy.mil

Darryll J. Pines

Smart Structures Laboratory, Alfred Gessow Rotorcraft Center, University of Maryland, College Park, MD 20742, USA

djpterp@eng.umd.edu

Michael Todd

Department of Structural Engineering, University of California, San Diego, 9500 Gilman Drive, Mail Code 0085, La Jolla, CA 92093-0085, USA

mdt@ucsd.edu

Jonathan M. Nichols

Code 5673, U.S. Naval Research Laboratory, Washington, DC 20375, USA

pele@ccs.nrl.navy.mil